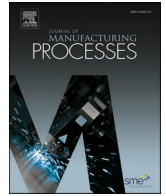




Contents lists available at ScienceDirect

Journal of Manufacturing Processes

journal homepage: www.elsevier.com/locate/manpro

High-throughput screening of surface roughness during additive manufacturing

Y. Du^a, T. Mukherjee^a, N. Finch^a, A. De^b, T. DebRoy^{a,*}

^a Department of Materials Science and Engineering, The Pennsylvania State University, University Park, PA 16802, USA

^b Department of Mechanical Engineering, Indian Institute of Technology, Bombay, Mumbai 400076, India

ARTICLE INFO

Keywords:

3D printing
Powder bed fusion
Heat transfer and fluid flow
Surface roughness
Dimensionless index
Buckingham pi-theorem

ABSTRACT

Smooth surfaces in the printed parts are essential for long fatigue life and high dimensional accuracy. They are currently achieved by post-process machining and grinding of external surfaces that add extra costs. Mitigating the surface roughness of internal channels remains a challenge. Here we use a high-throughput screening approach that analyzes the value of a dimensionless index for many experiments and provides a pathway for reducing the surface roughness without the need for post-processing. The index is derived by dimensional analysis of causative variables that affect the roughness of the surface such as heat input, powder diameter, layer thickness, pool aspect ratio, Marangoni force, contact angle, and enthalpy of melting of alloys. Using the results of high-throughput screening, we develop easy-to-use process maps that are consistent with the experimental observations. Among the causative variables, heat input and the contact angle of the molten material with the substrate have the highest and lowest influence on the smoothness of printed surfaces. An aluminum alloy, AlSi10Mg is found to be the best choice for printing smooth surfaces among the four alloys considered here. These findings can improve the surface quality of additively manufactured parts that now significantly hinder their wider industrial adaptation.

1. Introduction

3D printing or additive manufacturing (AM) of metals and alloys is widely used to fabricate complex and intricate parts for aerospace, energy, healthcare, transportation, and consumer product industries [1–6]. Thin layers of alloy powders are selectively melted by a high-intensity heat source such as a laser or electron beam and are solidified layer by layer to make intricate parts. These intricate parts mandate the printing of smooth surfaces to achieve fine geometry and high dimensional tolerance. However, the printed parts often suffer from rough surfaces [3,7,8] that affect the quality and dimensional accuracy of parts. In addition, rough surfaces may act as stress concentrating sites and initiate fatigue cracks and significantly degrade the mechanical performance and fatigue life of the parts [9,10]. Therefore, the printing of smooth surfaces is very important for fabricating dimensionally accurate, high-quality parts.

Several approaches have been undertaken to print smooth surfaces. Post-processing operations such as machining, grinding, and polishing produce smooth surfaces but add extra costs and are not applicable for finishing internal surfaces [11–13]. Hybrid manufacturing combines

deposition and machining to make smooth surfaces without the need for post-processing [14,15]. However, it is a slow and difficult process to control. Surface roughness can also be minimized by adjusting the process variables such as power and scanning speed of the laser beam, layer thickness, hatch spacing, and preheating temperature by experimental trial and error [16–18]. However, this process is time-consuming and expensive because it needs thousands of trial tests to explore a large window of process parameters. In addition, these experimental trials often do not guarantee smooth surfaces because surface roughness often does not follow a particular trend with the process variables. For example, low laser power may cause improper melting and rough surfaces; while a very high power may result in a high temperature which can cause spatter generation and poor surface finish [19–22]. Researchers have developed powder scale models that can simulate the formation of rough surfaces during AM [23]. However, these calculations are computationally intensive, require supercomputers available only in big companies and national labs, and are restricted to very small length and time scales.

Smooth surfaces can be printed using appropriate conditions to avoid surface roughness obtained by synthesizing a wide variety of available

* Corresponding author.

E-mail address: debroy@psu.edu (T. DebRoy).

<https://doi.org/10.1016/j.jmapro.2022.06.049>

Received 8 May 2022; Received in revised form 9 June 2022; Accepted 24 June 2022

1526-6125/© 2022 The Society of Manufacturing Engineers. Published by Elsevier Ltd. All rights reserved.

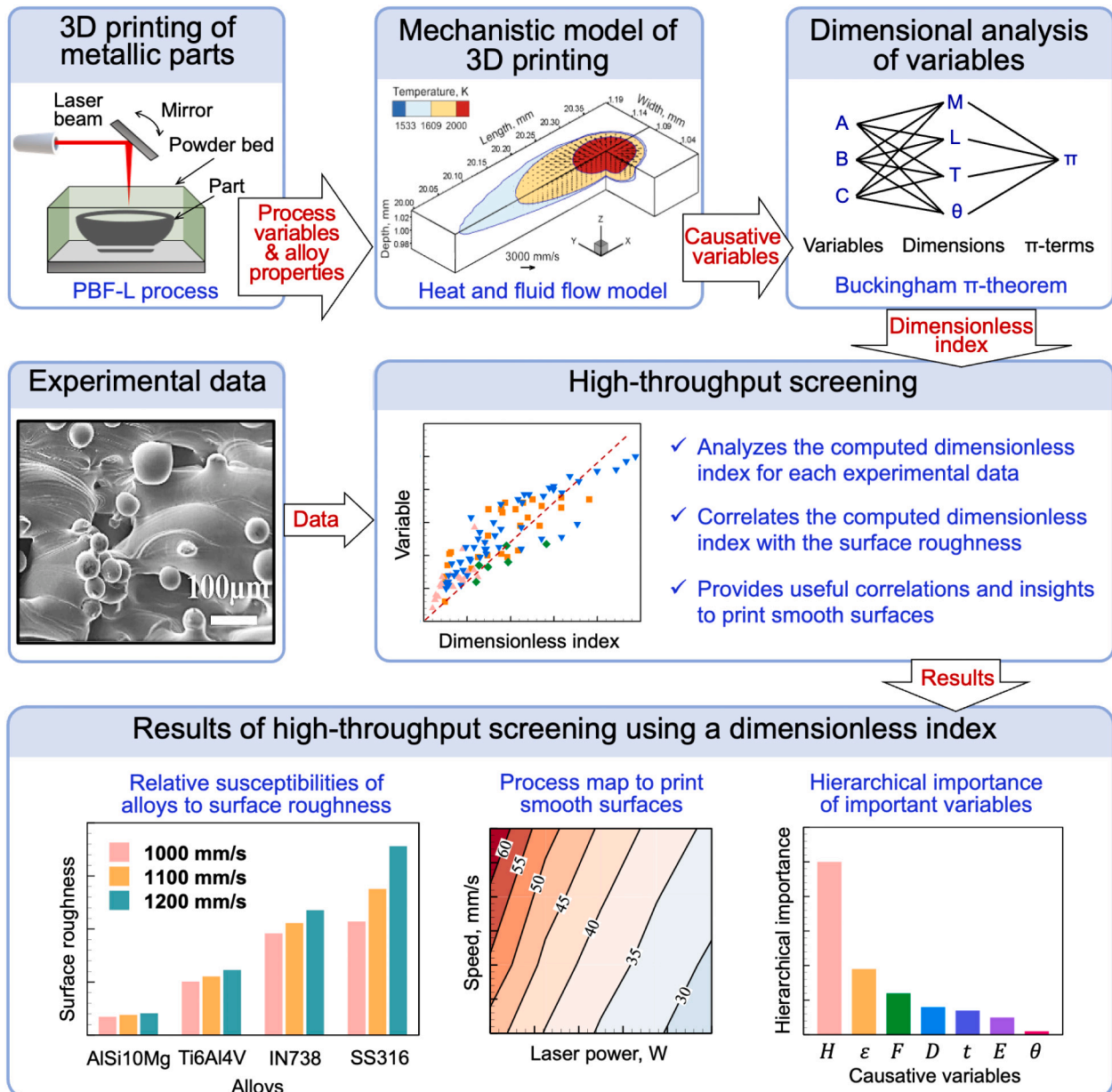


Fig. 1. Schematic representation of the method used. The high-throughput screening analyzes the values of a dimensionless index to provide important insights for printing smooth surfaces. The microstructural image showing the rough surfaces is taken from [31].

experimental data in a rapid and computationally efficient way. The high-throughput screening [24–28] approach can analyze a large volume of diverse data rapidly to provide important insights that cannot be obtained by any other means. It screens the available data based on the value of an index and makes useful predictions. An index is generally a dimensionless form of the combination of variables responsible for a particular problem. For example, a dimensionless quantity was used by correlating the variables representing the folding behavior of proteins such as molecular weight and the radius of gyration [29]. The high-throughput screening was used to analyze the values of the dimensionless quantity to assess the stability of proteins [29]. For the printing of smooth metallic surfaces, the dimensionless index can be derived by unifying the variables causing surface roughness. These causative variables include heat input [21,22], powder diameter [30], layer thickness [31], pool aspect ratio (pool length/depth) [32,33], Marangoni force [34], contact angle [35], and enthalpy of melting [3,4] of alloys and they depend on the AM process parameters and alloy properties.

Here we derive and propose a simple and verifiable dimensionless ‘surface roughness index’ by combining the causative variables for laser powder bed fusion (PBF-L) using the Buckingham π -theorem [36]. The values of the dimensionless index for one hundred and twenty independent experiments [31,37–49] for four alloys are computed and analyzed using a high-throughput screening method. The causative variables are calculated using a rigorously-tested heat transfer and fluid flow model of AM process [34,50]. The hierarchical influence of the causative variables on surface roughness is provided. In addition, different alloys are compared based on their relative susceptibility to surface roughness. Furthermore, we provide the surface roughness maps for four commonly used alloys under various conditions to guide the printing of smooth surfaces.

2. Methods

Fig. 1 explains the methodology used here. We identify several

Table 1
Variable, symbol, S.I. unit, dimension, range, and explanation of the variables used in SRI [3,21,22,30–35].

Variable	Symbol	S.I. unit	Dimension	Range	Explanation
Heat input	H	J/m	MLT^{-2}	6.67E+1–2.00E+3	Improper heat input may cause a discontinuous pool, form small metallic balls on the part surface, and result in rough surfaces. [21,22].
Powder diameter	D	m	L	9.00E-6–6.60E-5	Large powders can attach to the edge of the deposit and cause rough surfaces [30].
Layer thickness	t	m	L	2.00E-5–9.20E-5	Thick layers can increase the staircase effect and result in rough surfaces [31].
Pool aspect ratio	ϵ	–	–	1.40–14.50	Pools with a high aspect ratio are easy to break into discontinuous pools and can cause rough surfaces [32,33].
Marangoni force	F	N	MLT^{-2}	1.45E-6–3.17E-4	Large Marangoni force helps the spreading of liquid metal and is good for smooth surfaces [34].
Contact angle	θ	Radian	$M^0L^0T^0$	1.03–1.36	A large contact angle indicates difficulty in wetting and spreading that increases the surface roughness [35].
Enthalpy of melting	E	J/m ³	$ML^{-1}T^{-2}$	1.90E+9–7.10E+9	High enthalpy of melting may increase the amount of partially melted powders and result in rough surfaces [3].
Surface roughness	R_a	m	L	3.75E-6 – 3.58E-5	–

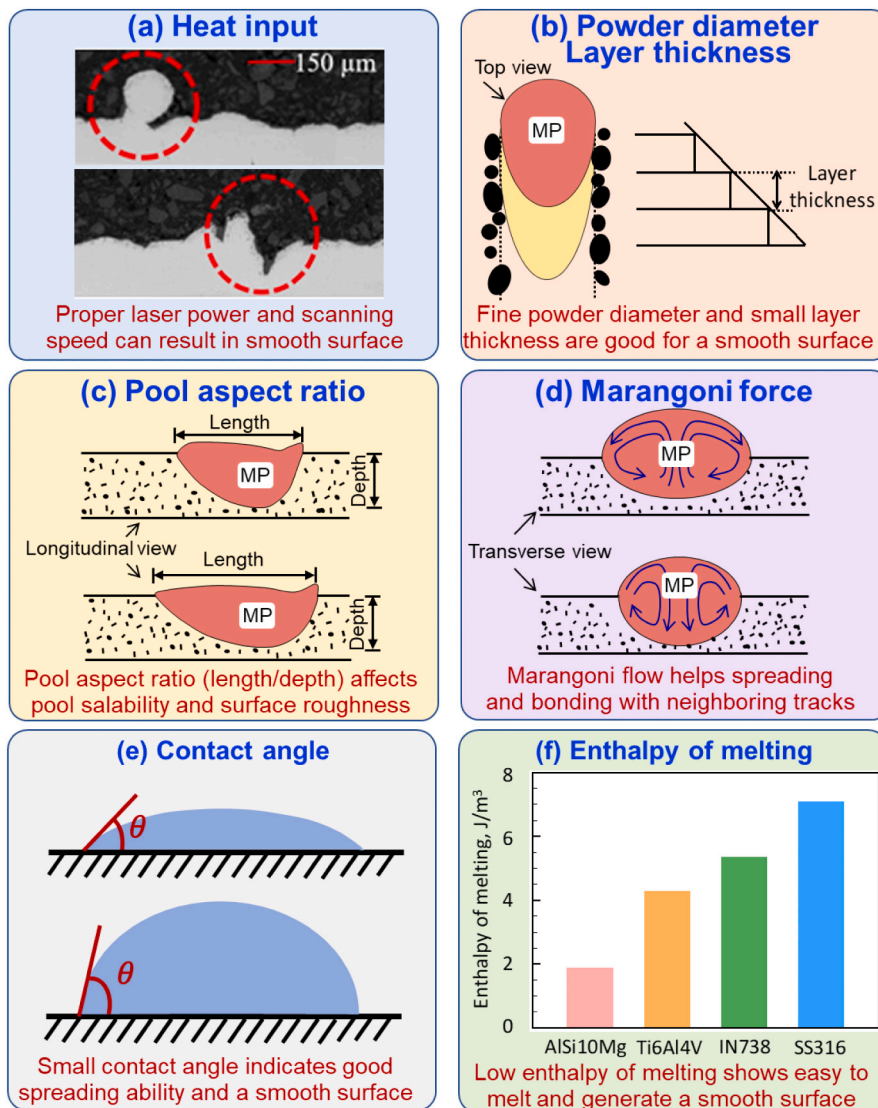


Fig. 2. Effect of the (a) heat input, (b) powder diameter and layer thickness, (c) pool aspect ratio, (d) Marangoni force, (e) contact angle, and (f) enthalpy of melting on surface roughness in PBF-L parts. The experimental results in (a) are taken from [21]. The values of enthalpy of melting for four alloys are taken from [3,4]. Explanations of the effects of these variables on the surface roughness are provided in Table 1.

causative variables for surface roughness including heat input per unit length of deposit (laser power/scanning speed) [21,22], powder diameter [30], and layer thickness [31] that are process variables, alloy properties such as enthalpy of melting [3] and contact angle [35], and mechanistic variables such as the aspect ratio of the pool (pool length/pool depth) [32,33] and Marangoni force [34]. Pool aspect ratio and Marangoni force are calculated using a heat transfer and fluid flow model of powder bed fusion [34,50]. The causative variables are combined in a dimensionless form using the Buckingham π theorem [36] to derive a surface roughness index (SRI). This index helps in high-throughput screening [24,25] of a large volume of experimental data to provide pathways to print parts with smooth surfaces.

2.1. Heat transfer and fluid flow model of powder bed fusion

A heat transfer and fluid flow model [34,50] is developed and used to calculate the pool size, temperature, and velocity fields during the PBF-L process taking the process parameters, material, and gas properties as inputs. The model iteratively solves the conservation equations of energy, mass, and momentum in a three-dimensional computational domain. An in-house Fortran code compiled using an Intel Fortran Compiler is used to perform the calculations in a 3D computational domain consisting of the substrate, power bed, deposited layers and hatches, and the shielding gas. The model provides accurate results on pool geometry and temperature fields by considering the effects of the convective flow of molten materials. A traveling grid approach [34] is used to enhance computational efficiency. More information about this model is available in previous publications [34,50]. The causative variables, the aspect ratio of the pool, and Marangoni force are calculated using this model.

2.2. Causative variables and their calculations

The causative variables (Table 1), their effects on the surface roughness (Fig. 2), and their calculation methods are explained in this sub-section. The values of the causative variables, material properties, and process parameters for one hundred and twenty independent experiments for four alloys are provided in Tables S1 and S2 in the Supplementary document.

2.2.1. Heat input (H)

In the PBF-L process, the laser is used as the heat source. The heat input is calculated as the ratio of laser power to scanning speed. High laser power and a low scanning speed provide high heat input. The heat input can affect the surface roughness (Fig. 2 (a)) by influencing the amount of molten liquid and the stability of the molten pool. Improper heat input, such as low laser power and a high scanning speed, results in an insufficient amount of molten liquid, improper pool size, a discontinuous deposit of liquid metal, and the formation of a rough surface [21]. However, too high heat input is also unfavorable for molten pool stability [22].

2.2.2. Powder diameter (D)

During PBF-L, partially-melted powders attached to the molten pool edge can cause a rough surface (Fig. 2 (b)). To reduce the influence of partially-melted powder attachment, the use of fine powders is often recommended [30]. However, small, uniform, and high-quality powders increase the cost. Some research suggests that the influence of the partially-melted powder attachment cannot be completely avoided [3]. A proper powder size should be selected to balance the surface quality and the feedstock cost.

2.2.3. Layer thickness (t)

The layer thickness plays an important role in the formation of rough surfaces. A high layer thickness increases the 'staircase effect' and increases the difficulty to build a smooth surface (Fig. 2 (b)) [31].

Therefore, the deposition of thin layers is recommended to reduce the surface roughness. However, a very small layer thickness indicates low productivity, requires more time to build a part and increases the cost. Therefore, a proper layer thickness should be selected to maintain a smooth surface without affecting productivity.

2.2.4. Pool aspect ratio (ϵ)

Rough surfaces may be originated because of the formation of balls due to the instability of the molten pool [32,33]. The capillary instability is related [33] to the pool aspect ratio which is represented as the ratio between the length and depth of the molten pool (Fig. 2 (c)). A molten pool with a long length and a small depth (high pool aspect ratio) is easy to separate into discontinuous parts, form balls around the deposit, and cause a rough surface [33]. Therefore, a small pool aspect ratio is helpful to reduce surface roughness. Both the length and depth of the pool are estimated using the heat transfer and fluid flow model to compute the values of the pool aspect ratio.

2.2.5. Marangoni force (F)

The surface roughness also depends on the molten liquid flow and pool geometry [4,34]. The spatial gradient of surface tension (in N/m), also called Marangoni stress (N/m²) primarily drives the convective flow of molten liquid. The liquid metal flows from the places with low values of surface tension to the places with high values. For a certain pool surface area, the integral of surface tension gradient or Marangoni stress over the pool top surface area is called Marangoni force (in N, Fig. 2 (d)). A high Marangoni force indicates a vigorous convective flow and uniform spreading of liquid, which is good for maintaining the continuity of the molten pool and forming a smooth surface. The Marangoni force (F) is determined as the product of the spatial gradient of surface tension (N/m²) and pool top surface area (m²) in Eq. (1). Surface tension gradient (τ) and pool top surface area (S_t) can be computed by the heat transfer and material flow model, shown in Eqs. (2) and (3), respectively.

$$F = \tau \times S_t, \quad (1)$$

$$\tau = -\frac{d\gamma}{dx} = -\frac{d\gamma}{dT} \times \frac{dT}{dx} = -\frac{d\gamma}{dT} \times \frac{\Delta T}{\Delta x} \quad (2)$$

$$S_t = \pi \times \frac{L}{2} \times \frac{W}{2} \quad (3)$$

where τ is the surface tension gradient (in N/m²), γ is the surface tension of the molten pool (in N/m), Δx is the distance along the pool surface, T is the temperature, ΔT is the difference of the peak temperature and the solidus temperature of alloys. S_t is the top surface area of the molten pool, which is assumed as a flat ellipse whose major and minor axes are equal to the pool length and width, respectively. Pool length and pool width are represented by L and W , respectively.

2.2.6. Contact angle (θ)

During the deposition of a layer, a molten liquid droplet spreads on the previously deposited tracks and the substrate, cools down and solidifies to form the deposit. The contact angle between the molten liquid droplet and the previously deposited tracks or the substrate affects the surface roughness [35]. The contact angle (Fig. 2 (e)) is measured as the angle of a liquid interacting with a solid surface. It affects the wetting and spreading ability of the molten liquid [35]. A low contact angle indicates that the liquid is easy to spread on the solid surface. Therefore, the alloy with a small contact angle is suitable for fabricating parts with smooth surfaces.

2.2.7. Enthalpy of melting (E)

Alloys with a low enthalpy of melting are easier to melt and form smooth surfaces [3,4]. Enthalpy of melting (Fig. 2 (f)) represents the heat required to melt per unit volume of material and is expressed as:

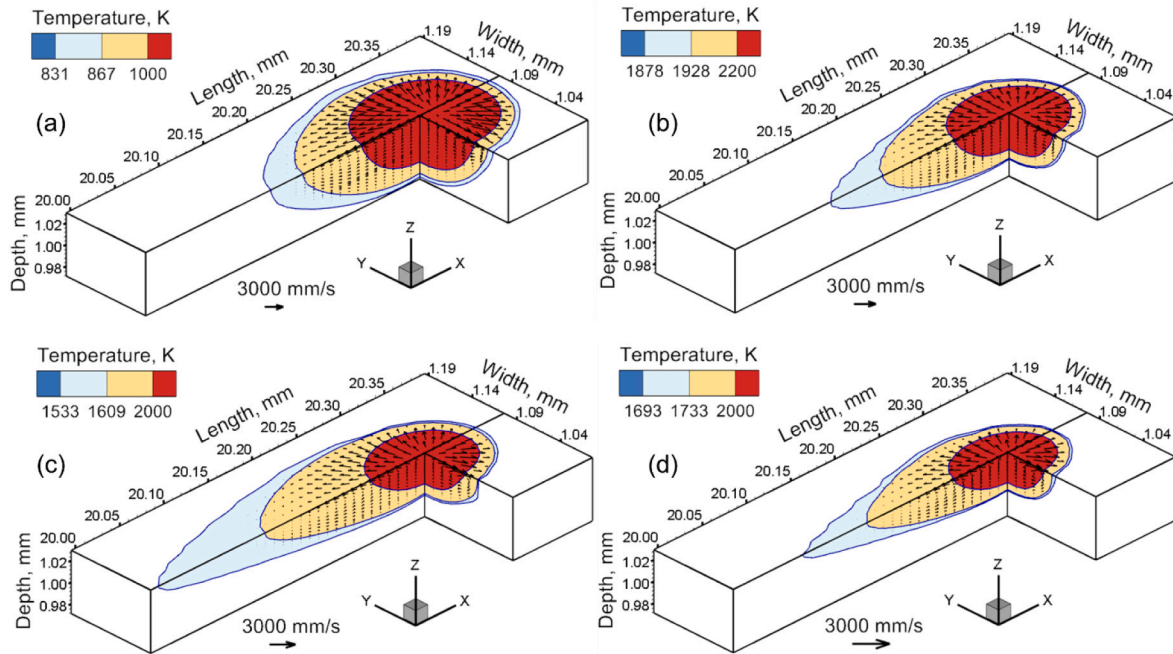


Fig. 3. 3D temperature and velocity distributions calculated using a heat transfer and fluid flow model for four alloys. The results are for 20 mm long single-track builds of (a) AlSi10Mg (b) Ti6Al4V (c) Inconel 738 (d) stainless steel 316 made by PBF-L using 60 W laser power, 1000 mm/s scanning speed and 30 μ m layer thickness and 50 μ m beam radius. The scanning direction of the laser beam is along the positive X direction. Y and Z directions represent the width and depth direction, respectively. Temperature values of the contour can be predicted from the temperature contour legend provided in each figure. Black arrows in the figures represent the velocity vectors whose magnitude can be estimated by comparing lengths with the reference vector provided.

$$E = \rho \times (c_p \times \Delta T + L) \quad (4)$$

where ρ and c_p are the density and the specific heat of alloys, respectively, ΔT is the temperature difference between the liquid and solidus temperatures, and L is the latent heat. The material properties of four alloys are available in Table S1 in the Supplementary document.

2.3. Buckingham π theorem for dimensional analysis

The aforementioned causative variables are combined using the Buckingham π theorem [36] in a dimensionless form. The theorem indicates that a physical equation with n number of physical variables can be rewritten in terms of p number of dimensionless parameters, $\pi_1, \pi_2, \pi_3, \dots, \pi_p$, constructed from the original equation, where k is the number of physical dimensions and $p = n - k$. The physical dimensions are mass (M), length (L), and time (T). For our case, we consider six variables ($n = 6$), $E, \theta, F, t, \epsilon,$ and H , and three dimensions, M, L, and T ($k = 3$). Therefore, there are three (6-3) dimensionless π terms. The variable, powder diameter (D) is used to non-dimensionalize the surface roughness where the roughness values are divided by the corresponding powder diameter. The Buckingham π theorem is used in this work for deriving a dimensionless surface roughness index.

2.4. Pearson's correlation matrix

For better understanding and analyzing data, the correlation between any two variables can be represented by Pearson's correlation coefficient [51] with the Eq. (5). The value of Pearson's correlation coefficient is in the range of $[-1, 1]$. The value closer to '1' indicates a stronger positive linear correlation between two variables (such as X and Y), while '-1' shows a perfect negative linear correlation. Values close to '0' suggest that two variables are independent of each other.

$$\rho = \frac{cov(X, Y)}{\sigma_X \sigma_Y} \quad (5)$$

where ρ is the Pearson's correlation coefficient, X and Y are two variables, $cov(X, Y)$ is the covariance of X and Y, σ_X and σ_Y are the standard deviations of X and Y, respectively. The calculations of covariance and standard deviation are explained in the Supplementary document. A Pearson's correlation matrix contains the correlation coefficients of all combinations of variables.

2.5. High-throughput screening

The high-throughput screening [24–28] approach can analyze a large volume of diverse data rapidly to provide important insights that cannot be obtained by any other means. It screens the available experimental data based on the value of the surface roughness index and makes useful predictions. Specifically, the values of the dimensionless surface roughness index corresponding to the one hundred and twenty experimental cases for four alloys are estimated. We screen the surface roughness index by comparing its computed values with the corresponding experimentally measured surface roughness. The screening approach provides a quantitative relation that can be used to reduce the surface roughness in printed parts.

3. Results and discussion

The formation of rough surfaces is affected by the temperature field as well as the geometry and dimensions of the molten pool. Under the same process condition, the molten pool shape, size, and temperature fields for the PBF-L process (Fig. 3) vary significantly for the four alloys used here. It indicates that the four alloys have different susceptibility to surface roughness. The results computed using the heat transfer and fluid flow model are validated using independent experimental results (Fig. 4). The calculated pool depth (Fig. 4 (a)) and pool width (Fig. 4 (b)) at different process conditions for four alloys agree well with the corresponding experimental results [52–56]. An excellent agreement between the computed and experimental data provides us the confidence to use the heat transfer and fluid flow model to accurately calculate the

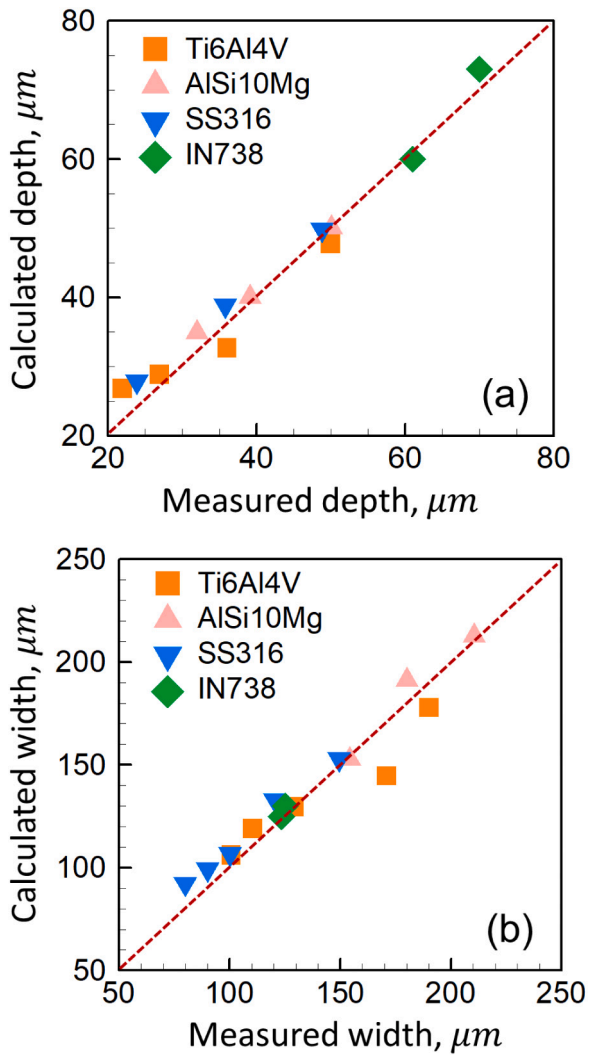


Fig. 4. Experimental validation of the heat transfer and fluid flow model of PBF-L. Comparison between the calculated and experimental measured (a) width and (b) depth of the molten pool of a single layer single hatch builds of Ti6Al4V, AlSi10Mg, stainless steel 316, and Inconel 738 at different linear heat inputs. The experimentally measured width and depth for stainless steel 316 are adapted from Di et al. [46] and Li et al. [52], respectively. The experimental results for Ti6Al4V and AlSi10Mg are taken from Gong et al. [53] and Kempen et al. [54], respectively. Gong et al. [53] and Kempen et al. [54] provided the macrograph from which Tang et al. [55] measured the dimensions. The experimental results for Inconel 738 are taken from [56].

causative variables. The causative variables responsible for surface roughness can be combined to provide a quantitative index that can be used for minimizing surface roughness. However, a prerequisite for deriving such an index is that the causative variables should be independent of each other. A Pearson’s correlation matrix [51] (see Section 2.4) shows that all variables have small values of correlation coefficients indicating that these variables are independent of each other (Fig. 5). These independent causative variables are used to derive a surface roughness index, as discussed below.

	E	t	ε	θ	H	F
E	1.00	-0.17	-0.15	0.01	0.22	-0.31
t	-0.17	1.00	-0.07	0.11	0.21	0.15
ε	-0.15	-0.07	1.00	0.25	-0.36	-0.01
θ	0.01	0.11	0.25	1.00	-0.03	0.01
H	0.22	0.21	-0.36	-0.03	1.00	0.18
F	-0.31	0.15	-0.01	0.01	0.18	1.00

Fig. 5. Pearson’s correlation coefficient matrix showing the inter-independence of the causative variables [51]. Details of these causative variables are provided in Table 1. The values indicate the correlation coefficient between variables. The absolute values of the correlation coefficient close to zero indicate that the variables are weakly correlated. In contrast, a high dependence between two variables is observed if the correlation coefficient between them is close to one.

3.1. Surface roughness index

The causative variables (Section 2.2) responsible for causing rough surfaces are combined in a dimensionless form using the Buckingham π theorem [36] to derive a surface roughness index (SRI) as shown in the Appendix as:

$$SRI = E t^2 (\varepsilon)^n \sqrt{\frac{\theta}{HF}} \tag{6}$$

where E , t , ε , θ , H , and F are enthalpy of melting (J/m^3), layer thickness (m), pool aspect ratio (pool length/depth), contact angle (radian), heat input (laser power/scanning speed, J/m), and Marangoni force (N). These causative variables, their symbols, S.I. units, dimensions, ranges, and influence on the surface roughness are provided in Table 1. The detailed derivation of the surface roughness index is provided in Appendix A. A high value of SRI points towards a high susceptibility to surface roughness. From Eq. (6), it is evident that a high pool aspect ratio results in a rough surface which is also consistent with the experimental observations (Fig. 6 (a)). The figure shows that the surface roughness is directly proportional to $\varepsilon^{0.25}$, which provides the value of the constant ‘n’ in Eq. (6) as 0.25. Similarly, the linear proportionality of the surface roughness with $(1/H)^{0.5}$ and $(1/F)^{0.5}$ is also consistent with the experimental data, as shown in Fig. 6 (b) and (c), respectively. Since surface roughness decreases at higher values of the heat input (H) and Marangoni force (F) (Section 2.2), these two variables are in the denominator in Eq. (6). In addition, an increase in enthalpy of melting (E), layer thickness (t), and contact angle (θ) enhance the surface roughness (Section 2.2). Therefore, these three variables are also in the numerator in Eq. (6).

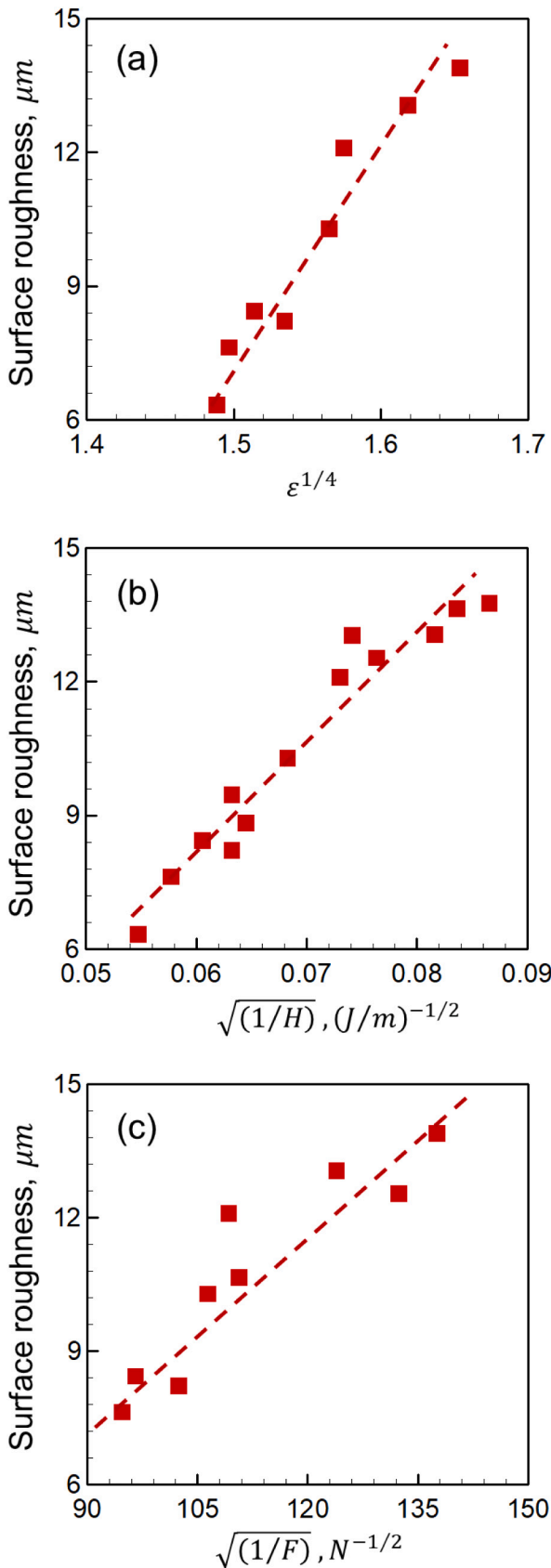


Fig. 6. Variations of experimentally measured surface roughness (R_a) with the causative variables. Variations of surface roughness with (a) pool aspect ratio (ϵ), (b) heat input (H), and (c) Marangoni force (F), and for stainless steel 316 in PBF-L. The experimental surface roughness results are taken from [46] where average values of surface roughness are reported.

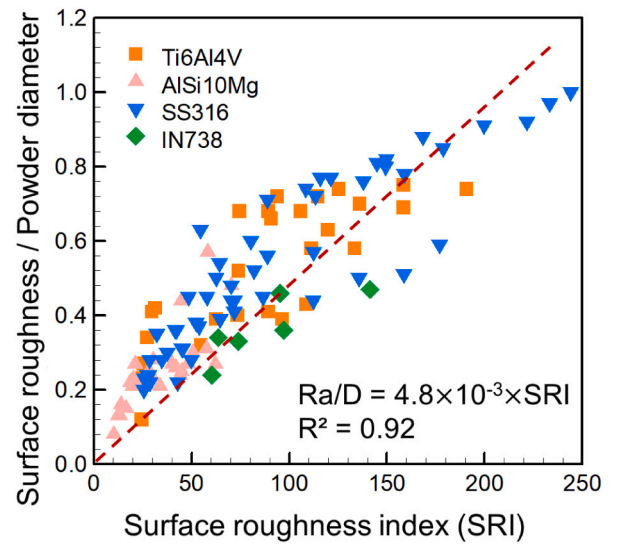


Fig. 7. Variation of the surface roughness/powder diameter (R_a/D) as a function of surface roughness index (SRI). The plot is made using 120 independent experimental data for four commonly used alloys. The experimental surface roughness results are collected from literature [31,37–49]. The corresponding values of SRI are calculated using Eq. (6). The coefficient of 4.8×10^{-3} is a data fitting constant value. The process parameters and material properties for surface roughness index calculation for 120 independent experimental data are provided in Tables S1 and S2 in the Supplementary document. The R^2 value of 0.92 indicates a good linear fitting.

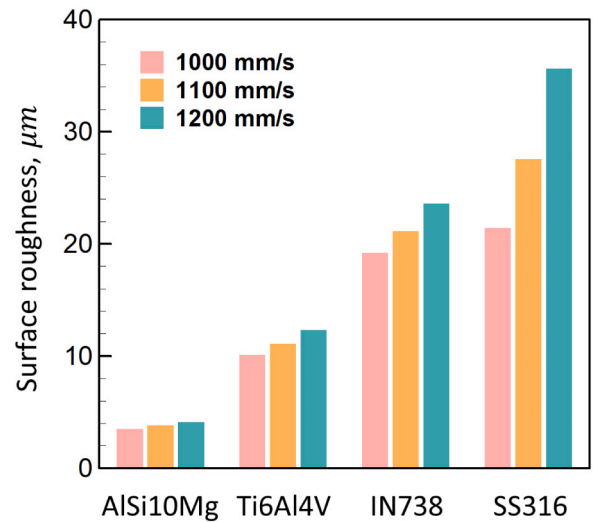
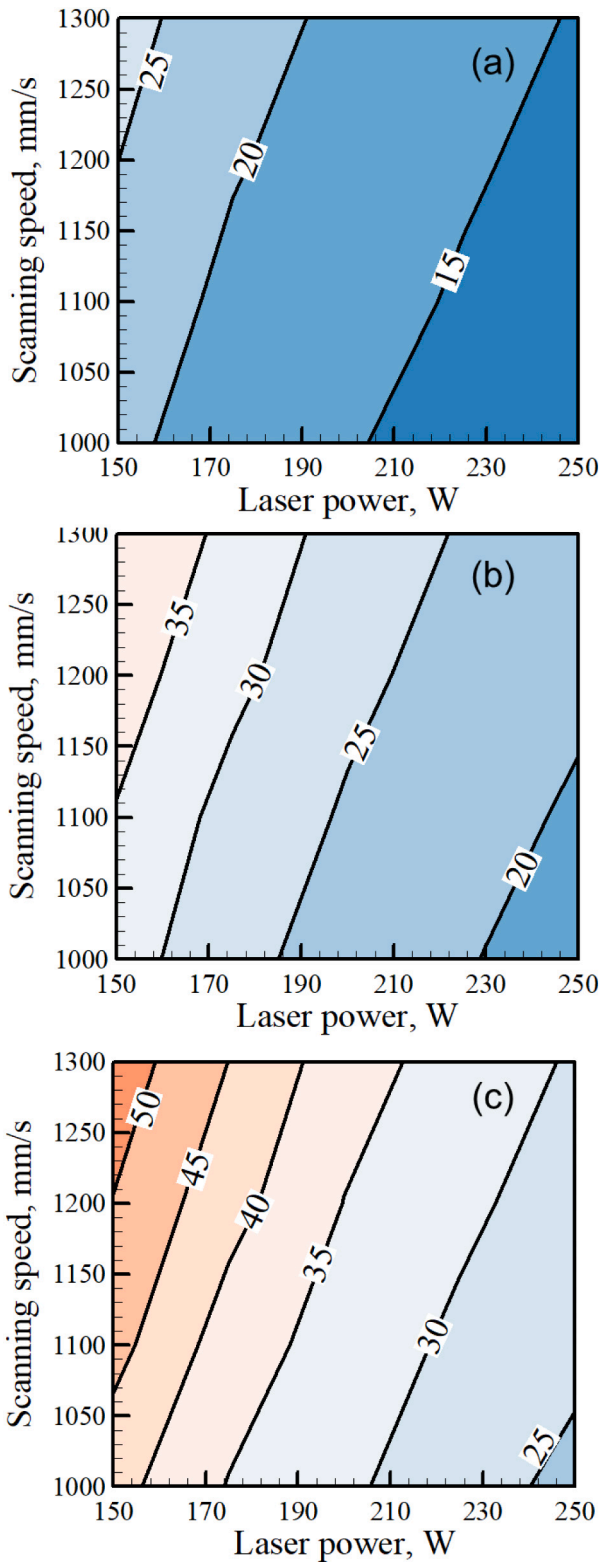


Fig. 8. Relative susceptibilities of alloys to surface roughness. Variation of the surface roughness index for the four alloys at various process conditions. Values of the surface roughness were calculated for AlSi10Mg, Inconel 738, Ti6Al4V, and stainless steel 316 builds using Eq. (7). Three different scanning speeds of 1000 mm/s, 1100 mm/s, and 1200 mm/s are calculated respectively, with powder diameter of $30 \mu\text{m}$, laser power of 250 W, the beam diameter of $100 \mu\text{m}$, and layer thickness of $40 \mu\text{m}$.

Fig. 7 shows that the computed values of SRI for one hundred and twenty data points for four alloys follow a linear trend with the corresponding values of experimentally measured surface roughness [31,37–49]. Here, the surface roughness (R_a) values are non-dimensionalized by dividing them with the corresponding values of



(caption on next column)

Fig. 9. Surface roughness maps for Ti6Al4V for various powder sizes. Surface roughness maps show the variations in the surface roughness (R_a) value with laser power and scanning speeds for three different powder diameters (a) 20, (b) 30, and (c) 40 μm . The layer thickness for all three figures is 40 μm . The values on the contour lines represent the values of surface roughness, in μm , computed using Eq. (7). The surface roughness results are for 20 mm long single-track builds of Ti6Al4V alloy made by PBF-L. Surface roughness values increase with increasing scanning speed, decreasing laser power, and increasing powder diameter. The trends of the surface roughness maps are consistent with the common industrial practice for both fusion welding and additive manufacturing. Ranges of process parameters are available in Table 1. The process parameters and material properties for surface roughness index calculation for 120 independent experimental data are provided in Table S2 in the Supplementary document.

powder diameter (D). Both the surface roughness (R_a) and powder diameter (D) have the unit of the meter (Table 1) and their ratio (R_a/D) is a dimensionless quantity. The linear fitting (Fig. 7) is expressed by an equation as:

$$\frac{R_a}{D} = K \times SRI = K E t^2 (\epsilon)^n \sqrt{\frac{\theta}{H F}} \quad (7)$$

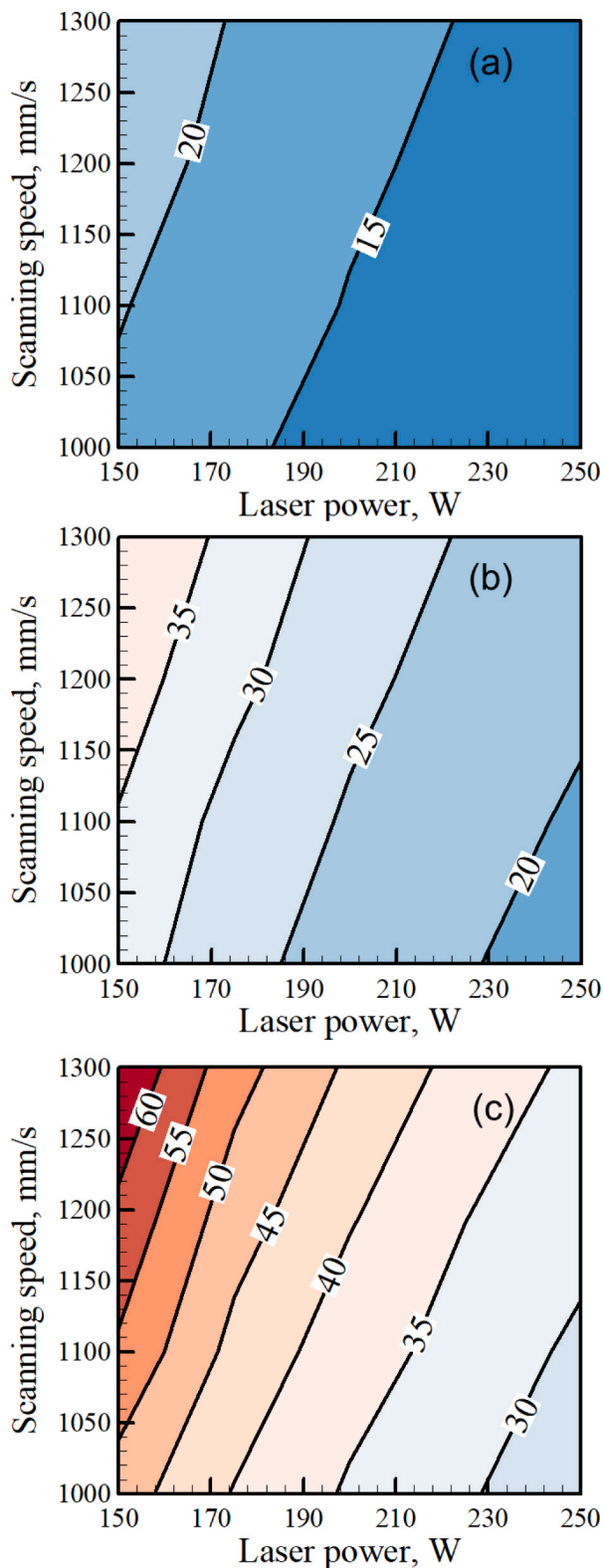
where R_a and D are surface roughness (m) and powder diameter (m), respectively. K is the slope of the linear plot (Fig. 7) which is equal to 0.0048 and the value of the constant n is 0.25. The plot of (R_a/D) vs. SRI is a linear plot passing through the origin (Fig. 7) indicating a perfectly smooth surface for a value of SRI equals zero. Eq. (7) is valid for the four alloys and the range of the variables provided in Table 1. For a new part, causative variables are needed to be computed for the corresponding processing conditions. Subsequently, those calculated values should be used in Eq. (7) to estimate surface roughness. To include a new alloy, Eq. (7) needs to be modified by incorporating new experimental data for that alloy. The one hundred and twenty experimental surface roughness [31,37–49] and corresponding process parameters and calculated causative variables are provided in Table S2 in the Supplementary document. The surface roughness index (SRI) provides a usable scale to compute and compare the values of surface roughness at different processing conditions and alloys, as discussed below.

3.2. Relative susceptibility of alloys to surface roughness

Fig. 8 compares the computed values of SRI for four commonly used alloys, SS316, Ti6Al4V, IN738, and AlSi10Mg at different scanning speeds of 1000, 1100, and 1200 mm/s while other process parameters are kept constant. For the same process condition, the AlSi10Mg alloy has the lowest value of SRI , indicating the least susceptibility to surface roughness among the four alloys (Fig. 8). This is primarily attributed to the lowest values of pool aspect ratio (Fig. 3) and enthalpy of melting (Fig. 2 (f)) of AlSi10Mg among the four alloys. In contrast, high values of pool aspect ratio and enthalpy of melting of SS 316 make it the most vulnerable to surface roughness among the four alloys (Fig. 8). Fig. 8 also shows that rapid scanning increases surface roughness for all four alloys. This is because rapid scanning reduces the heat input (H) which increases the surface roughness (Eq. 7). Similar to the scanning speed, other process variables such as laser power, layer thickness, and powder diameter also significantly affect the surface roughness. Surface roughness maps showing the variations in surface roughness with these process variables can be useful to engineers for predicting the surface roughness before experiments, as discussed below.

3.3. Surface roughness maps

Computed values of surface roughness (in μm) using Eq. (7) at different combinations of processing conditions are used to construct



(caption on next column)

Fig. 10. Surface roughness maps for Ti6Al4V for various layer thicknesses. Surface roughness maps show the variations in the surface roughness (R_a) value with laser power and scanning speeds for three different layer thicknesses (a) 30, (b) 40, and (c) 50 μm . The powder diameter for all three figures is 30 μm . The values on the contour lines represent the values of surface roughness, in μm , computed using Eq. (7). The surface roughness results are for 20 mm long single-track builds of Ti6Al4V alloy made by PBF-L. Surface roughness values increase with increasing scanning speed, decreasing laser power, and increasing layer thickness. The trends of the surface roughness maps are consistent with the common industrial practice for both fusion welding and additive manufacturing. Ranges of process parameters are available in Table 1. The process parameters and material properties for surface roughness index calculation for 120 independent experimental data are provided in Table S2 in the Supplementary document.

surface roughness maps (Figs. 9 and 10). For each sub-figure, it is obvious that the surface roughness values increase with an increase in scanning speed or reduction in laser power. Apart from the scanning speed and laser power, powder diameter and layer thickness also play important roles in determining the surface roughness. In Fig. 9 (a-c), the surface roughness increases for larger powder diameter, which agrees well with the influence of partial melted powders attachment on surface roughness as explained in Table 1. The attachment of the bigger size partial melted powders to the molten pool edge shows more difficulty in producing a smooth surface. In Fig. 10 (a-c), thicker layers increase the surface roughness. The ‘staircase effect’ is more pronounced with a larger layer thickness. The surface roughness maps for the other three alloys, AlSi10Mg, Inconel 738, and Stainless steel 316 are presented in Fig. 11. Once the surface roughness maps are available on the shop floor for an alloy, engineers can predict the surface roughness before performing any experiments. From Figs. 8–11, it is evident that the surface roughness varies significantly depending on the processing conditions and alloys used. The combined effects of processing conditions and alloy properties on surface roughness are captured using the causative variables in Eq. (7). However, these causative variables do not equally contribute to creating rough surfaces. Their relative influence on surface roughness is very important because it can guide engineers to know which variable to adjust to reduce surface roughness, as discussed below.

3.4. Hierarchical importance of causative variables on surface roughness

To estimate the hierarchy of the importance of the causative variables on surface roughness, each variable is varied by 20% of their ranges [57] (Table 1) and the variation in the coefficient of determination (R^2) for the linear fitting in Fig. 7 is calculated. The calculated values of the new R^2 are compared with the original value of R^2 (0.92 in Fig. 7). The variable with the highest change of R^2 (represented in percentage change in Fig. 12) shows the highest influence on surface roughness. Fig. 12 shows that the heat input and pool aspect ratio are the first and second most important variables affecting the surface roughness. Heat input impacts both the amount of liquid and the stability of the molten pool, which shows the critical and decisive influence on surface roughness. The second important variable, the pool aspect ratio, represents the shape, capillary stability, and continuity of the molten pool, also shows an important influence on surface roughness. The contact angle is found as the least important variable. The contact angle is a material property which is a constant value for a specific alloy and is very limited to represent the complex mechanisms of evolution of rough surfaces. The hierarchy of the importance of the causative variables on surface roughness guides the engineers and researchers to identify which variables need to be adjusted [58,59] to print parts with smooth surfaces using PBF-L.

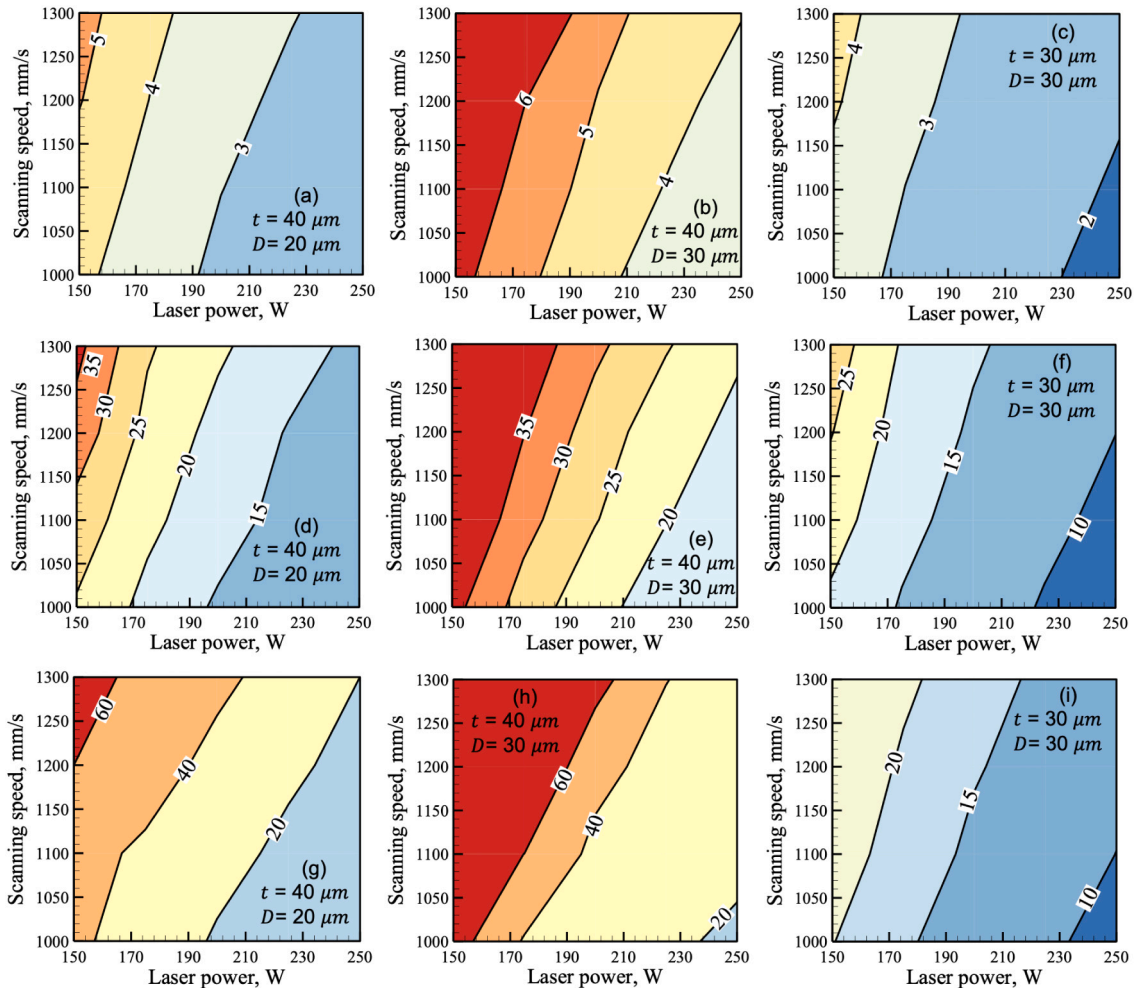


Fig. 11. Surface roughness maps for (a-c) AlSi10Mg, (d-f) IN738, and (g-i) SS316 for various layer thicknesses (t) and powder diameters (D). Surface roughness maps show the variations in the surface roughness (R_a) value with laser power and scanning speeds for three different layer thicknesses (t) 30, 40, and 50 μm , three different powder diameters (D) 20, 30, and 40 μm . The values on the contour lines represent the values of surface roughness, in μm , computed using Eq. (7). The surface roughness results are for 20 mm long single-track builds of AlSi10Mg, IN738, and SS316 alloys made by PBF-L. Surface roughness values increase with increasing scanning speed, decreasing laser power, and increasing layer thickness and powder diameter. The trends of the surface roughness maps are consistent with the common industrial practice for both fusion welding and additive manufacturing. Ranges of process parameters are available in Table 1. The process parameters and material properties for surface roughness index calculation for 120 independent experimental data are provided in Table S2 in the Supplementary document.

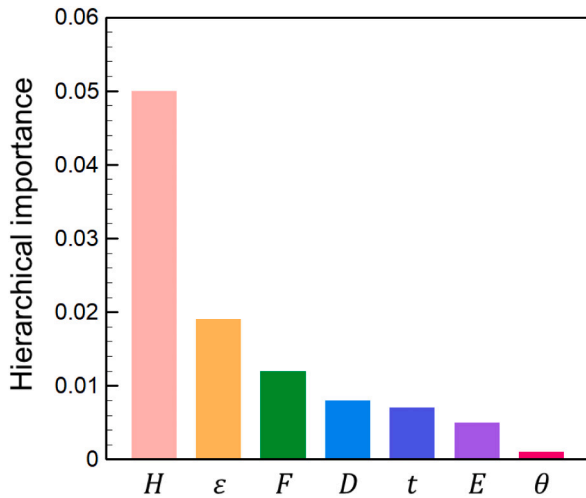


Fig. 12. Hierarchical importance of variables on surface roughness. The hierarchical importance is evaluated by varying each variable by 10% of their ranges (Table 1) and calculating the variation in the coefficient of determination (R^2) for the linear fitting in Fig. 7, and comparing that with the 0.92 (R^2 before variation in Fig. 7). The variable with the highest change of R^2 (represented in percentage change) shows the highest influence on surface roughness. The heat input and pool aspect ratio are found as the first and second most important variables contributing to the surface roughness. The calculations are performed using 120 independent experimental data [31,37–49].

4. Summary and conclusions

We derive and propose a dimensionless ‘surface roughness index’ during laser powder bed fusion, which is the ratio of the extent of roughness divided by the powder diameter. We compute several causative variables using a rigorously-tested heat transfer and fluid flow model of powder bed fusion for one hundred and twenty independent experiments with four alloys, SS316, Ti6Al4V, IN738, and AlSi10Mg. We analyze the surface roughness index using a high-throughput screening method to provide pathways to print smooth surfaces. The effectiveness of the method is established using data from independent

Appendix A. The derivation of the surface roughness index (SRI)

The six causative variables, heat input, layer thickness, pool aspect ratio, Marangoni force, contact angle, and enthalpy of melting, are used to derive the dimensionless surface roughness index using the Buckingham π theorem [36]. The other causative variable, powder diameter (D) is used to non-dimensionalize the surface roughness where the roughness values are divided by the corresponding powder diameter. Since there are 3 fundamental dimensions (M, L, and T) and six variables, there are three ($6-3=3$) π terms. These π terms (π_1 , π_2 , and π_3) are dimensionless. For the π terms, there should be three repeating and three non-repeating variables. The three repeating variables are chosen to be F , t , and H . Applying Buckingham π -theorem, the three π terms can be written as,

$$\pi_1 = (F)^{a_1} (t)^{b_1} (H)^{c_1} (E) \quad (8)$$

$$\pi_2 = (F)^{a_2} (t)^{b_2} (H)^{c_2} (\varepsilon) \quad (9)$$

$$\pi_3 = (F)^{a_3} (t)^{b_3} (H)^{c_3} (\theta) \quad (10)$$

where the π terms are dimensionless ($M^0L^0T^0$), and the values of the exponents (a , b , and c) for each π term need to be found out by equating the dimensions in Eqs. 8, 9, and 10. The three π terms are calculated as,

$$\pi_1 = \frac{E t^2}{\sqrt{HF}} \quad (11)$$

$$\pi_2 = \varepsilon \quad (12)$$

$$\pi_3 = \theta \quad (13)$$

The surface roughness index (SRI) is represented as:

experiments. Below are the specific findings:

- (1) A dimensionless surface roughness index (SRI) is derived and validated by one hundred and twenty independent experimental data collected from the literature. This dimensionless index combines the mechanisms of surface roughness formation, including the influence of heat input, powder diameter, layer thickness, pool aspect ratio (pool length/depth), Marangoni force, contact angle, and enthalpy of melting of alloys on the surface roughness.
- (2) The heat input per unit length of the deposit is found as the most important variable affecting the surface roughness due to its critical importance in determining the amount of liquid and stability of the molten pool. The pool aspect ratio represents the shape and stability of the molten pool and is found as the second most important variable.
- (3) AlSi10Mg is the least susceptible to surface roughness among the four alloys under the same processing conditions. This is primarily attributed to the lowest values of pool aspect ratio, lowest enthalpy of melting, and highest Marangoni force for AlSi10Mg. In addition, the stainless steel 316 is the most susceptible alloy to surface roughness.
- (4) We provide surface roughness maps for four commonly used alloys, SS316, Ti6Al4V, IN738, and AlSi10Mg, using the dimensionless index where the variations in the surface roughness with the common PBF-L variables are consistent with the common practice in the additive manufacturing industry.

Data availability statement

The raw/processed data required to reproduce these findings cannot be shared at this time due to technical or time limitations.

Declaration of competing interest

The authors declare that they have no known competing financial interests or personal relationships that could have appeared to influence the work reported in this paper.

$$SRI = \pi_1 (\pi_2)^n \sqrt{\pi_3} = E t^2 (\epsilon)^n \sqrt{\frac{\theta}{HF}} \quad (14)$$

where E , t , ϵ , θ , H , and F are enthalpy of melting (J/m^3), layer thickness (m), pool aspect ratio (pool length/depth), contact angle (radian), heat input (laser power/scanning speed, J/m), and Marangoni force (N). The value of the exponent 'n' is estimated from the linear fitting as 0.25 (in Fig. 6 (a)).

Appendix B. Supplementary data

Supplementary data to this article can be found online at <https://doi.org/10.1016/j.jmapro.2022.06.049>.

References

- DebRoy T, Mukherjee T, Wei HL, Elmer JW, Milewski JO. Metallurgy, mechanistic models and machine learning in metal printing. *Nat Rev Mater* 2021;6(1):48–68. <https://doi.org/10.1038/s41578-020-00236-1>.
- DebRoy T, Mukherjee T, Milewski JO, Elmer JW, Ribic B, Blecher JJ, et al. Scientific, technological and economic issues in metal printing and their solutions. *Nat Mater* 2019;18(10):1026–32. <https://doi.org/10.1038/s41563-019-0408-2>.
- DebRoy T, Wei HL, Zuback JS, Mukherjee T, Elmer JW, Milewski JO, et al. Additive manufacturing of metallic components—process, structure and properties. *Prog Mater Sci* 2018;92:112–224. <https://doi.org/10.1016/j.pmatsci.2017.10.001>.
- Wei HL, Mukherjee T, Zhang W, Zuback JS, Knapp GL, De A, et al. Mechanistic models for additive manufacturing of metallic components. *Prog Mater Sci* 2021;116:100703. <https://doi.org/10.1016/j.pmatsci.2020.100703>.
- Gu D, Shi X, Poprawe R, Bourell DL, Setchi R, Zhu J. Material-structure-performance integrated laser-metal additive manufacturing. *Science* 2021;372(6545):eabg1487. <https://www.science.org/doi/10.1126/science.abg1487>.
- Bhadeshia HK, DebRoy T. *Innovations in everyday engineering materials. First ed.* Switzerland: Springer; 2021.
- Molaei R, Fatemi A, Phan N. Notched fatigue of additive manufactured metals under axial and multiaxial loadings, part I: effects of surface roughness and HIP and comparisons with their wrought alloys. *Int J Fatigue* 2021;143:106003. <https://doi.org/10.1016/j.ijfatigue.2020.106003>.
- Ghosh A, Kumar A, Wang X, Kietzig AM, Brochu M. Analysis of the effect of surface morphology on tensile behavior of LPBF SS316L microstruts. *Mater Sci Eng A* 2022;831:142226. <https://doi.org/10.1016/j.msea.2021.142226>.
- Hasib MT, Ostergaard HE, Liu Q, Li X, Kruzic JJ. Tensile and fatigue crack growth behavior of commercially pure titanium produced by laser powder bed fusion additive manufacturing. *Addit Manuf* 2021;45:102027. <https://doi.org/10.1016/j.addma.2021.102027>.
- Shrestha R, Sirmsiriwong J, Shamsaei N. Fatigue behavior of additive manufactured 316L stainless steel under axial versus rotating-bending loading: synergistic effects of stress gradient, surface roughness, and volumetric defects. *Int J Fatigue* 2021;144:106063. <https://doi.org/10.1016/j.ijfatigue.2020.106063>.
- Maleki E, Bagherifard S, Bandini M, Guagliano M. Surface post-treatments for metal additive manufacturing: Progress, challenges, and opportunities. *Addit Manuf* 2021;37:101619. <https://doi.org/10.1016/j.addma.2020.101619>.
- Velu R, Balan AS, Mazumder J. Laser aided metal additive manufacturing and postprocessing: a comprehensive review. *Addit Manuf* 2021:427–56. <https://doi.org/10.1016/B978-0-12-818411-0.00023-9>.
- Mahmood MA, Chioibasu D, Ur Rehman A, Mihai S, Popescu AC. Post-processing techniques to enhance the quality of metallic parts produced by additive manufacturing. *Metals* 2022;12(1):77. <https://doi.org/10.3390/met12010077>.
- Mak SY, Tam KL, Yung CH, Yau WF. Hybrid metal 3D printing for selective polished surface. In: *Materials science forum*. 1027. Trans Tech Publications Ltd; 2021. p. 136–40. <https://doi.org/10.4028/www.scientific.net/MSF.1027.136>.
- Wüst P, Edelmann A, Hellmann R. Areal surface roughness optimization of maraging steel parts produced by hybrid additive manufacturing. *Materials* 2020;13(2):418. <https://doi.org/10.3390/ma13020418>.
- Bhardwaj T, Shukla M, Prasad NK, Paul CP, Bindra KS. Direct laser deposition-additive manufacturing of Ti–15Mo alloy: effect of build orientation induced surface topography on corrosion and bioactivity. *Met Mater Int* 2020;26(7):1015–29. <https://doi.org/10.1007/s12540-019-00464-3>.
- Cooke S, Ahmadi K, Willerth S, Herring R. Metal additive manufacturing: technology, metallurgy and modelling. *J Manuf Process* 2020;57:978–1003. <https://doi.org/10.1016/j.jmapro.2020.07.025>.
- Nayak SK, Mishra SK, Jinoop AN, Paul CP, Bindra KS. Experimental studies on laser additive manufacturing of Inconel-625 structures using powder bed fusion at 100 μm layer thickness. *J Mater Eng Perform* 2020;29(11):7636–47. <https://doi.org/10.1007/s11665-020-05215-9>.
- Esmailizadeh R, Ali U, Keshavarzkermani A, Mahmoodkhani Y, Marzbanrad E, Toyserkani E. On the effect of spatter particles distribution on the quality of hastelloy X parts made by laser powder-bed fusion additive manufacturing. *J Manuf Process* 2019;37:11–20. <https://doi.org/10.1016/j.jmapro.2018.11.012>.
- Young ZA, Guo Q, Parab ND, Zhao C, Qu M, Escano LI, et al. Types of spatter and their features and formation mechanisms in laser powder bed fusion additive manufacturing process. *Addit Manuf* 2020;36:101438. <https://doi.org/10.1016/j.addma.2020.101438>.
- Zhang X, Zheng Y, Suresh V, Wang S, Li Q, Li B, et al. Correlation approach for quality assurance of additive manufactured parts based on optical metrology. *J Manuf Process* 2020;53:310–7. <https://doi.org/10.1016/j.jmapro.2020.02.037>.
- De Oliveira Campos F, Araujo AC, Munhoz ALJ, Kapoor SG. The influence of additive manufacturing on the micromilling machinability of Ti6Al4V: a comparison of SLM and commercial workpieces. *J Manuf Process* 2020;60:299–307. <https://doi.org/10.1016/j.jmapro.2020.10.006>.
- Francois MM, Sun A, King WE, Henson NJ, Tourret D, Bronkhorst CA, et al. Modeling of additive manufacturing processes for metals: challenges and opportunities. *Curr Opin Solid State Mater Sci* 2017;21(4):198–206. <https://doi.org/10.1016/j.cossms.2016.12.001>.
- Curtarolo S, Hart GL, Nardelli MB, Mingo N, Sanvito S, Levy O. The high-throughput highway to computational materials design. *Nat Mater* 2013;12(3):191–201. <https://doi.org/10.1038/nmat3568>.
- Pegues JW, Melia MA, Puckett R, Whetten SR, Argibay N, Kustas AB. Exploring additive manufacturing as a high-throughput screening tool for multiphase high entropy alloys. *Addit Manuf* 2021;37:101598. <https://doi.org/10.1016/j.addma.2020.101598>.
- Melia MA, Whetten SR, Puckett R, Jones M, Heiden MJ, Argibay N, et al. High-throughput additive manufacturing and characterization of refractory high entropy alloys. *Appl Mater Today* 2020;19:100560. <https://doi.org/10.1016/j.apmt.2020.100560>.
- Moorehead M, Bertsch K, Niezgoda M, Parkin C, Elbakhshwan M, Sridharan K, et al. High-throughput synthesis of mo-nb-ta-w high-entropy alloys via additive manufacturing. *Mater Des* 2020;187:108358. <https://doi.org/10.1016/j.matdes.2019.108358>.
- Go J, Schiffes SN, Stevens AG, Hart AJ. Rate limits of additive manufacturing by fused filament fabrication and guidelines for high-throughput system design. *Addit Manuf* 2017;16. <https://doi.org/10.1016/j.addma.2017.03.007>. 1–1.
- Pohl C, Mahapatra S, Kulakova A, Streicher W, Peters GH, Nørgaard A, et al. Combination of high throughput and structural screening to assess protein stability—a screening perspective. *Eur J Pharm Biopharm* 2022;171:1. <https://doi.org/10.1016/j.ejpb.2021.08.018>.
- Khairallah SA, Anderson AT, Rubenchik A, King WE. Laser powder-bed fusion additive manufacturing: physics of complex melt flow and formation mechanisms of pores, spatter, and denudation zones. *Acta Mater* 2016;108:36–45. <https://doi.org/10.1016/j.actamat.2016.02.014>.
- Qiu C, Panwisawas C, Ward M, Basoalto HC, Brooks JW, Attallah MM. On the role of melt flow into the surface structure and porosity development during selective laser melting. *Acta Mater* 2015;96:72–9. <https://doi.org/10.1016/j.actamat.2015.06.004>.
- Johnson L, Mahmoudi M, Zhang B, Seede R, Huang X, Maier JT, et al. Assessing printability maps in additive manufacturing of metal alloys. *Acta Mater* 2019;176:199–210. <https://doi.org/10.1016/j.actamat.2019.07.005>.
- Du Y, Mukherjee T, DebRoy T. Physics-informed machine learning and mechanistic modeling of additive manufacturing to reduce defects. *Appl Mater Today* 2021;24:101123. <https://doi.org/10.1016/j.apmt.2021.101123>.
- Mukherjee T, Wei HL, De A, DebRoy T. Heat and fluid flow in additive manufacturing—Part I: modeling of powder bed fusion. *Comput Mater Sci* 2018;150:304–13. <https://doi.org/10.1016/j.commatsci.2018.04.022>.
- Tyagi P, Goulet T, Riso C, Stephenson R, Chuenprateep N, Schlitzer J, et al. Reducing the roughness of internal surface of an additive manufacturing produced 316 steel component by chempolishing and electropolishing. *Addit Manuf* 2019;25:32–8. <https://doi.org/10.1016/j.addma.2018.11.001>.
- Bird RB, Stewart WE, Lightfoot EN. *Transport phenomena*. 2nd ed. New York: John Wiley & Sons; 2006.
- Khorasani AM, Gibson I, Ghasemi A, Ghaderi A. Modelling of laser powder bed fusion process and analysing the effective parameters on surface characteristics of ti-6Al-4V. *Int J Mech Sci* 2020;168:105299. <https://doi.org/10.1016/j.jimecs.2019.105299>.
- Oyesola M, Mpofu K, Mathe N, Fatoba S, Hoosain S, Daniyan I. Optimization of selective laser melting process parameters for surface quality performance of the fabricated Ti6Al4V. *Int J Adv Manuf Technol* 2021;114(5):1585–99. <https://doi.org/10.1007/s00170-021-06953-3>.
- Li Z, Kucukkoc I, Zhang DZ, Liu F. Optimising the process parameters of selective laser melting for the fabrication of Ti6Al4V alloy. *Rapid Prototyp J* 2018;24(1):150–9. <https://doi.org/10.1108/RPJ-03-2016-0045>.
- Fatemi A, Molaei R, Sharifimehr S, Phan N, Shamsaei N. Multiaxial fatigue behavior of wrought and additive manufactured ti-6Al-4V including surface finish effect. *Int J Fatigue* 2017;100:347–66. <https://doi.org/10.1016/j.ijfatigue.2017.03.044>.
- Calignano F, Manfredi D, Ambrosio EP, Iuliano L, Fino P. Influence of process parameters on surface roughness of aluminum parts produced by DMLS. *Int J Adv Manuf Technol* 2013;67(9):2743–51. <https://doi.org/10.1007/s00170-012-4688-9>.

- [42] Maamoun AH, Xue YF, Elbestawi MA, Veldhuis SC. Effect of selective laser melting process parameters on the quality of al alloy parts: powder characterization, density, surface roughness, and dimensional accuracy. *Materials* 2018;11(12):2343. <https://doi.org/10.3390/ma11122343>.
- [43] Balbaa MA, Ghasemi A, Fereiduni E, Elbestawi MA, Jadhav SD, Kruth JP. Role of powder particle size on laser powder bed fusion processability of AlSi10Mg alloy. *Addit Manuf* 2021;37:101630. <https://doi.org/10.1016/j.addma.2020.101630>.
- [44] Taute C, Möller H, Du Plessis A, Tshibhalanganda M, Leary M. Characterization of additively manufactured AlSi10Mg cubes with different porosities. *J South Afr Inst Min Metall* 2021;121(4):143–50. <https://doi.org/10.17159/2411-9717/1331/2021>.
- [45] Badrossamay M, Yasa E, Van Vaerenbergh J, Kruth JP. Improving productivity rate in SLM of commercial steel powders. *Tech Pap Soc Manuf Eng* 2009;1–3. <https://irias.kuleuven.be/1580214?limo=0>.
- [46] Wang D, Liu Y, Yang Y, Xiao D. Theoretical and experimental study on surface roughness of 316L stainless steel metal parts obtained through selective laser melting. *Rapid Prototyp J* 2016;22(4):706–16. <https://www.emerald.com/insight/content/doi/10.1108/RPJ-06-2015-0078>.
- [47] Cao L, Li J, Hu J, Liu H, Wu Y, Zhou Q. Optimization of surface roughness and dimensional accuracy in LPBF additive manufacturing. *Opt Laser Technol* 2021;142:107246. <https://doi.org/10.1016/j.optlastec.2021.107246>.
- [48] Fleming TG, Nestor SG, Allen TR, Boukhalel MA, Smith NJ, Fraser JM. Tracking and controlling the morphology evolution of 3D powder-bed fusion in situ using inline coherent imaging. *Addit Manuf* 2020;32:100978. <https://doi.org/10.1016/j.addma.2019.100978>.
- [49] Guo C, Li S, Shi S, Li X, Hu X, Zhu Q, et al. Effect of processing parameters on surface roughness, porosity and cracking of as-built IN738LC parts fabricated by laser powder bed fusion. *J Mater Process Technol* 2020;285:116788. <https://doi.org/10.1016/j.jmatprotec.2020.116788>.
- [50] Mukherjee T, Wei HL, De A, DebRoy T. Heat and fluid flow in additive manufacturing—Part II: powder bed fusion of stainless steel, and titanium, nickel and aluminum base alloys. *Comput Mater Sci* 2018;150:369–80. <https://doi.org/10.1016/j.commatsci.2018.04.027>.
- [51] Jebli I, Belouadha FZ, Kabbaj MI, Tilioua A. Prediction of solar energy guided by Pearson correlation using machine learning. *Energy* 2021;224:120109. <https://doi.org/10.1016/j.energy.2021.120109>.
- [52] Li R, Shi Y, Wang Z, Wang L, Liu J, Jiang W. Densification behavior of gas and water atomized 316L stainless steel powder during selective laser melting. *Appl Surf Sci* 2010;256(13):4350–6. <https://doi.org/10.1016/j.apsusc.2010.02.030>.
- [53] Gong H, Gu H, Zeng K, Dilip JJ, Pal D, Stucker B. Melt pool characterization for selective laser melting of ti-6Al-4V pre-alloyed powder. *Solid Freeform Fabr Symp* 2014:256–67. <https://doi.org/10.26153/tsw/15682>.
- [54] Kempen K, Thijs L, Van Humbeeck J, Kruth JP. Processing AlSi10Mg by selective laser melting: parameter optimisation and material characterisation. *Mater Sci Technol* 2015;31(8):917–23. <https://doi.org/10.1179/1743284714Y.0000000702>.
- [55] Tang M, Pistorius PC, Beuth JL. Prediction of lack-of-fusion porosity for powder bed fusion. *Addit Manuf* 2017;14:39–48. <https://doi.org/10.1016/j.addma.2016.12.001>.
- [56] Grange D, Queva A, Guillemot G, Bellet M, Bartout JD, Colin C. Effect of processing parameters during the laser beam melting of inconel 738: comparison between simulated and experimental melt pool shape. *J Mater Process Technol* 2021;289:116897. <https://doi.org/10.1016/j.jmatprotec.2020.116897>.
- [57] Dixit M, Parejiya A, Essehli R, Muralidharan N, Haq SU, Amin R, et al. SolidPAC is an interactive battery-on-demand energy density estimator for solid-state batteries. *Cell Rep Phys Sci* 2022;3(2):100756. <https://doi.org/10.1016/j.xcrp.2022.100756>.
- [58] Scime L, Beuth J. A multi-scale convolutional neural network for autonomous anomaly detection and classification in a laser powder bed fusion additive manufacturing process. *Addit Manuf* 2018;24:273–86. <https://doi.org/10.1016/j.addma.2018.09.034>.
- [59] Maleki E, Bagherifard S, Guagliano M. Application of artificial intelligence to optimize the process parameters effects on tensile properties of ti-6Al-4V fabricated by laser powder-bed fusion. *Int J Mech Mater Des* 2022;18(1):199–222. <https://doi.org/10.1007/s10999-021-09570-w>.

Y. Du received a Bachelor of Engineering degree in Materials Science and Engineering from the Lanzhou University of Technology, China, in 2013, Master of Engineering and Ph. D. degrees in Materials Science and Engineering from Tianjin University, China in 2020. This research was done when she was at the Department of Materials Science and Engineering of the Pennsylvania State University. Currently, she is a postdoctoral researcher at Princeton University. Her research interests include additive manufacturing, friction stir welding, numerical modeling, heat and mass transfer, thermal distortion and residual stress, mechanical properties assessment, and machine learning.

T. Mukherjee is a Postdoctoral Researcher at the Pennsylvania State University where he earned his Ph.D. in Materials Science and Engineering. His research interests include additive manufacturing, welding, machine learning, multi-physics modeling, heat and mass transfer, thermal distortion, and residual stress. He has published several papers in leading international journals including *Nature Reviews Materials*, *Nature Materials*, and *Progress in Materials Science*. He has recently edited a book entitled “The Science and Technology of 3D Printing” and served as a Guest Editor for the journals “Computational Materials Science” and “Materials”.

N. Finch is a Ph.D. student at the Department of Materials Science and Engineering at the Pennsylvania State University. Before that, he got his bachelor’s degree from Penn State. His research interests include heat transfer and fluid flow, additive manufacturing, and numerical modeling.

A. De is a Professor of Mechanical Engineering and a former Academic Dean at the Indian Institute of Technology, Bombay. His research interests include fusion welding, friction stir welding, additive manufacturing, heat transfer and fluid flow, numerical modeling, residual stresses, and distortion. He has published many papers in international peer-reviewed journals, book chapters, and conference proceedings. He is also an Editor of the journal “Science and Technology of Welding and Joining”.

T. DebRoy is a Professor of Materials Science and Engineering at Penn State and the author of 370 papers, 5 edited books, and a 2021 book on “Innovations in Everyday Engineering Materials.” He has served as a Fulbright Distinguished Chair in Brazil, Distinguished Visiting Professor at IIT Bombay, Aditya Birla Chair at IISc, Bangalore, UK Royal Academy of Engineering Distinguished Visiting Fellow at Cambridge University, and Visiting Professor at KTH, Stockholm. He is a Founding Editor of the journal “Science and Technology of Welding and Joining.”